Ab-initio study of atomic structure and mechanical behaviour of *Al*/*Fe* intermetallic interfaces

Muhammad Zeeshan Khalid[a,b,*], Jesper Friis[c,d], Per Harald Ninive[a], Knut Marthinsen[b], Are Strandlie[a]

[a] *Department of Manufacturing and Civil Engineering, Norwegian University of Science and Technology, Gjøvik, 2815, Norway*
[b] *Department of Materials Science and Engineering, Norwegian University of Science and Technology (NTNU), Norway*
[c] *SINTEF Materials and Chemistry, Trondheim, Norway*
[d] *Department of Physics, Norwegian University of Science and Technology, Trondheim, Norway*

ABSTRACT

First-principles virtual tensile and shear test calculations have been performed to $Al(00\bar{3})//\alpha\text{-AlFeSi}(001)$ and $Al(0\bar{1}4)//Fe_4Al_{13}(10\bar{1})$ interfaces by the ab initio pseudo potential density functional theory method. Work of separation, ultimate tensile strength and shear strength of bulk and interface structures were calculated. The $Al(00\bar{3})//\alpha\text{-AlFeSi}(001)$ interface showed higher tensile strength than the $Al(0\bar{1}4)//Fe_4Al_{13}(10\bar{1})$ interface structure. Moreover, interface calculations revealed a charge depletion region in the second layer of the Fe_4Al_{13} structure, which caused lower work of separation. Furthermore, shear calculations showed stronger shear strength for the $Al(0\bar{1}4)//Fe_4Al_{13}(10\bar{1})$ interface than for the $Al(001)//\alpha\text{-AlFeSi}(001)$ interface structure.

1. Introduction

Steel and aluminum alloys have been regarded as some of the most promising combinations of alloys in industrial applications due to the possibility of combining high strength and low weight. Thus joining of aluminum and steel has gained immense industrial interest in several sectors such as, aeronautics [1], automotive [2], tooling [3], power generation [4] and marine applications [5]. However, the main challenge is the ability to efficiently join this combination of metals due to the differences in the physical and chemical properties of aluminum and steel. Due to the phase diagram of the Al-Fe system with several intermetallic phases, it is also impossible to avoid the development of Fe-Al Intermetallic Compounds (IMCs) [6,7]. Based on the temperature reached during the welding process in addition to alloy types and cooling rates, a large variety of IMCs can be created at the interface [8,9]. Hence, it is necessary to explore the effect of these IMCs on the joint strength to achieve a better understanding and overview of different welding methodologies.

Several studies have investigated the role and formation of intermetallic layers at aluminum and steel joints [10–13]. It has been generally reported that Fe-rich IMCs such as FeAl and Fe_3Al are less brittle than Al-rich IMCs, like Fe_4Al_{13} [10]. Although it has been generally accepted that the presence of IMC layers at the interface has detrimental effects on the joint strength, some of the studies have

nevertheless reported that Fe-rich IMCs may improve the mechanical properties and therefore do not have a detrimental effect on the strength of joints [11–13]. Assuming role of IMCs can have both negative and positive effects on the mechanical properties of joints.

Liu and Dunlop [9] studied the intermetallic phases including Fe_4Al_{13}, bcc α-AlFeSi, $FeAl_m$, q_1-AlFeSi and q_2-AlFeSi. They determined the crystallographic orientation relationships between Fe_4Al_{13}, bcc α-AlFeSi, and q_n-AlFeSi (n = 1,2) with Al using electron diffraction.

Chen et al. [14] reported three different types of failure modes: (i) button pullout failure, which is failure caused by shear displacement, (ii) bulk IMCs failure, and (iii) interfacial failure, i.e. failure at the interface of the aluminum and steel joint. In general, the understanding of the role of IMCs on the joint strength is ambiguous and far from complete. One of the reasons for the lack of detailed information about interfacial strength is the difficulty in characterizing the individual interfacial layers due to their small size. Over the years, many researchers have tried to identify and characterize the layers using Scanning Electron Microscopy (SEM), X-ray diffraction, and Transmission Electron Microscopy (TEM) [9,15–17]. McDevitt et al. [15] characterized the commercially produced hot-dip galvanized steel by using a combination of analytical TEM, SEM and X-ray diffraction. They reported the presence of Fe_2Al_5 and Fe_4Al_{13} IMCs at the Al//steel interface and concluded that X-ray diffraction is best suited for characterizing the interfacial layers. Recently, Arbo et al. [17] reported three

---

distinct phases: α-AlFeSi, Fe_4Al_{13} and Fe_2Al_5 at an aluminum-steel joint by TEM.

All these experiments reported that several possible phases may exist between aluminum alloys and steel, but little work has been done on quantifying the interfacial strength of these IMCs. As mentioned above, this is mainly due to the small size of the intermetallic layers. Due to experimental limitations and challenges, there has been a growing interest in computational approaches. To predict the mechanical and bonding strength, a wide range of theoretical methodologies have been applied, including semi-empirical and tight binding atomistic calculation methods, thermodynamic models, image models, and ab initio calculations using Hartree-Fock (HF) and Density Functional Theory (DFT) [18]. Some researchers performed atomistic simulations to calculate the mechanical and structural properties of the Fe-Al bulk intermetallic compounds [19–22]. All these methods show good agreement with available experiments, in particular the DFT approaches. But, according to our knowledge, nobody has studied the interfacial characteristics of the Al//Fe_4Al_{13} and Al//α-AlFeSi interfaces.

In this work, we have studied the interfacial structure and mechanical strength of Fe_4Al_{13} and cubic α-AlFeSi intermetallic phases with pure aluminum through atomistic simulations using DFT. We have developed the interface structures by finding the minimum misfit orientation between Al//α-AlFeSi and Al//Fe_4Al_{13} interface structures.

This paper is organized as follows. First, we discuss the methods, which comprise the computational methodology and the method to produce interface structures. In this part, we first make comparisons of bulk calculations of individual bulk phases with experiments and literature, which we further use for interface building. We then discuss the tensile and shear strength of the relevant interfaces, which comprise the most interesting feature of this work, followed by a discussion of the implications and significance of these results. We finally make a summary and present conclusions of our work.

2. Methods

2.1. Computational method

We performed first-principles calculations based on density functional theory using the Vienna Ab-initio Simulation Package (VASP) code [23] using the Generalized Gradient Approximation (GGA) by Projector Augmented-Wave method (PAW) [24] employing the Perdew-Burke-Ernzerhof (PBE) approach [25]. For Al, Fe and Si atoms, the electronic states $3s^23p^1$, $3d^64s^2$ and $3s^23p^2$, respectively, were treated as valence electrons. For calculations, a cutoff of 550 eV for the plane wave expansion of the wave function was used to obtain accurate forces. Automatic k-points were generated by using the method by Monkhorst and Pack [26]. The electronic convergence criteria were set to 1×10^{-5} eV, and maximum forces on each ion during relaxation were 0.005 eV/Å for bulk and 0.01 eV/Å for the interface structures.

2.2. Interface structures

The atomic positions and lattice constants of α-AlFeSi and Fe_4Al_{13} were directly taken from a study published by Cooper [27] and Liu and Dunlop [9]. The DFT-relaxed bulk structures were used further for interface building. The lattice parameters used for the building of interface structures are given in Table 1. Following a face-to-face matching technique, we found the following low misfit orientation relationships:

$[010]_{Fe_4Al_{13}} \| [200]_{Al}$
$[10\bar{1}]_{Fe_4Al_{13}} \| [041]_{Al}$
$(10\bar{1})_{Fe_4Al_{13}} \| (0\bar{1}4)_{Al}$ and
$[100]_{\alpha} \| [310]_{Al}$
$[010]_{\alpha} \| [1\bar{3}0]_{Al}$
$(001)_{\alpha} \| (00\bar{3})_{Al}$.

The corresponding $Al(0\bar{1}4)$//$Fe_4Al_{13}(10\bar{1})$ and $Al(00\bar{3})$//α-AlFeSi

Table 1
Lattice constants of the Al, Fe_4Al_{13} and b.c.c. α-AlFeSi phases, as calculated in this work and from literature.

Compound	Space group	a (Å)	b (Å)	c (Å)	Angle
Al	Fm-3 m	4.04	4.04	4.04	$\alpha = \beta = \gamma = 90°$
Fe_4Al_{13}	C2/m	15.49	8.08	12.48	$\alpha = 90°$,
		15.532[20]	8.010[20]	12.398[20]	$\beta = 107.7°$,
		15.069[19]	7.864[19]	12.083[19]	$\gamma = 90°$
		15.49[9]	8.083[9]	12.476[9]	
α-AlFeSi	Im3	12.69	12.69	12.69	$\alpha = \beta = \gamma = 90°$
		12.56[9]	12.56[9]	12.56[9]	
		12.589[28]	12.589[28]	12.589[28]	

$(00\bar{1})$ bulk and overlapped interface structures are shown in Fig. 1.

A vacuum layer of > 10 Å was introduced along the z-direction to avoid periodic interaction between interfaces. At least 6 layers of aluminum and the relevant intermetallic compound were considered in our calculations to reduce surface effects.

Liu and Dunlop [9] also studied and reported Orientation Relationships (OR) for Al//Fe_4Al_{13} interfaces and claimed $[020]_{Al}$ // $[010]_{Fe_4Al_{13}}$ to be the lowest mismatch direction due to the higher possible symmetry of the intersection group (2/m). They reported a mismatch of 0.18% along the $[020]_{Al}$ // $[010]_{Fe_4Al_{13}}$ direction.

In the case of the $Al(001)$//α-AlFeSi(001) interface, both lattice directions were equally strained. The lattice mismatch between Al and α-AlFeSi was found to be 0.89% for the OR studied in this paper (Table 2). Due to the small lattice mismatch, this $Al(00\bar{3})$//α-AlFeSi (001) interface orientation is a likely OR for the Al//α-AlFeSi interface structure.

The matched interface structures are shown in Fig. 2. Fig. 2(a) and (c) show the un-relaxed strained interface structures. The DFT optimized structures are shown in Fig. 2 (b), and (d), and these were used further for the virtual tensile and shear tests.

3. Interface strength calculations

3.1. Ideal work of separation

The ideal work of separation is the reversible work required to separate the interfaces into free surfaces, ignoring the plastic and diffusion degrees of freedom. It is defined as [29,30]:

$$W_{sep} = \frac{E_1^{tot} + E_2^{tot} - E_{12}^{tot}}{A} \tag{1}$$

where E_i^{tot} is the total energy of the constituent slab, E_{12}^{tot} is the total energy of the interface, and A is the interface area. To make consistent comparisons of constituent slabs and the interface, the shape and volume of the slabs and interface remain the same. Table 3 lists the work of separation of $Al(00\bar{3})$//α-AlFeSi(001) and $Al(0\bar{1}4)$//$Fe_4Al_{13}(10\bar{1})$ interfaces.

Under tensile load, a fracture can occur at the different interface layers. Thus it is necessary to calculate the work of separation W_{sep} inside the different layers and compare it with the work of separation W_{sep} at the interface. W_{sep} at the interface and different interface layers are defined as 0 and ± 1, ±2, ±3, respectively, while bulk Al and bulk IMC are W_{sep} for pure bulk Al and IMCs. An illustration is shown in Fig. 3. Since the interfacial strength is defined at the weakest point of the interface structure, this comparison will give indications of the location of the most vulnerable zone [30].

W_{sep} was calculated for both Al metal and the IMCs α-AlFeSi and Fe_4Al_{13}. We calculated W_{sep} for the fracture between Al//IMC counting from interfaces between first, second and third layers, represented as +1, +2, and +3 from the Al side and −1, −2 and −3 from the IMC side, respectively. Generally, the IMCs were found to have higher W_{sep} than Al except for the second layer of Fe_4Al_{13} (1.15 J/m^2). Therefore,
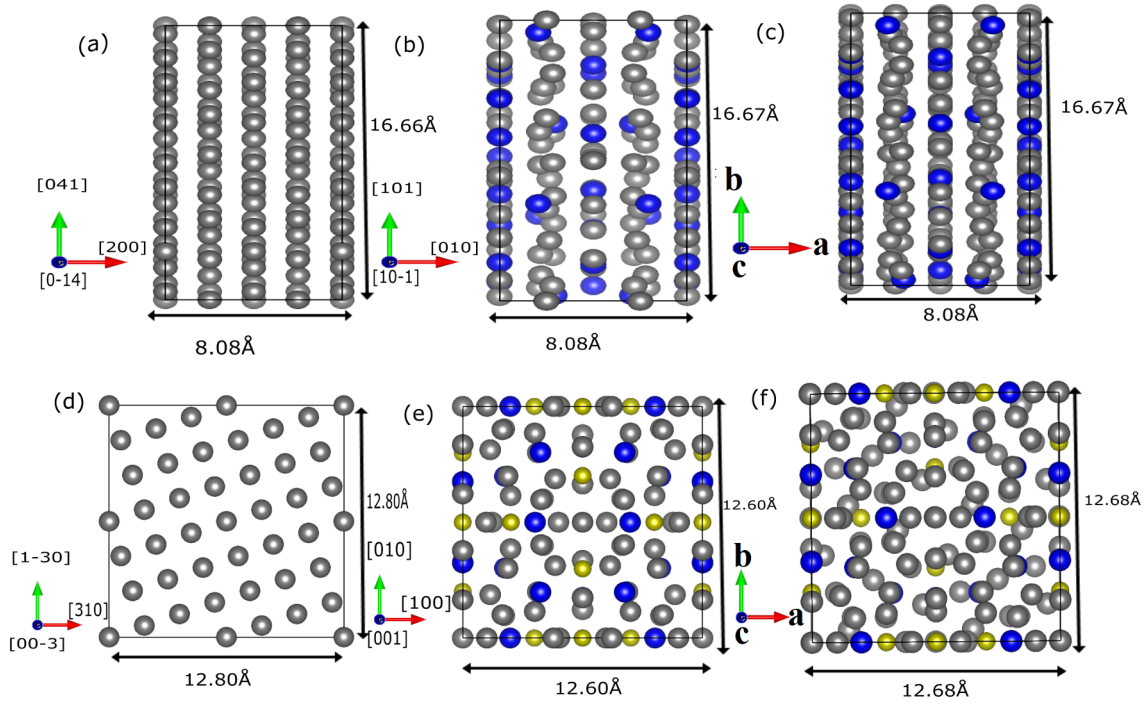
Fig. 1. The atomic arrangement of Al (a, d), Fe_4Al_{13} (b) and b.c.c. α-AlFeSi (e). Overlapping structures of Al and Fe_4Al_{13}, (c) and α-AlFeSi, (f) are shown according to the orientation relationship of the bulk phases.

Table 2
Lattice strain for Al//Fe_4Al_{13} and Al//α-AlFeSi interfaces. In the table the angles are defined as $\Delta\gamma = \gamma_2 - \gamma_1$.

	Strain along a (%)	Strain along b (%)	Difference in angle ($\Delta\gamma$)
Al(1 0 0)//Fe_4Al_{13}(1 0 0)	0.0	0.10	$\Delta\gamma = 0.0°$
Al(0 0 1)//α-AlFeSi(0 0 1)	0.89	0.89	$\Delta\gamma = 0.0°$

the second layer (-2) of Fe_4Al_{13} can be assumed to be the weakest zone of the overall Al//Fe_4Al_{13} interface. This weakening effect of Fe_4Al_{13} can be caused by charge depletion from the second layer towards the interface side. The charge density plot in subsection 3.6 further explains the reason for this lower value of W_{sep}. Overall, Fe_4Al_{13} showed higher W_{sep} than the α-AlFeSi phase, with the highest value reported to be 4.08 J/m^2 at the -1 side of the IMC.

For the Al//α-AlFeSi interface, W_{sep} is larger at the interface than in Al, implying that the fracture is more likely to occur inside the Al metal. The W_{sep} at $+2$ was noted to be the smallest compared to the other layers of metal. For the Al//Fe_4Al_{13} interface, W_{sep} was also found to be larger at the interface, implying that the interfacial strength of Al//Fe_4Al_{13} is higher at the interface than in the Al side. For both interface structures, W_{sep} showed a lower value for the bulk IMC and bulk Al, as compared to W_{sep} at the interface.

Moreover, to define a baseline, Al// IMC values were compared with the pure Al// Fe interface structure. Al// Fe interface showed a higher value of W_{sep} (5.84 J/m^2) [31] than Al// IMC interfaces, which indicates the presence of IMCs have a detrimental effect on the aluminum and steel joint.

3.2. Virtual tensile test calculations

Ab-initio tensile calculations of Al//Fe_4Al_{13} and Al//α-AlFeSi interfaces were carried out in the framework of the Rigid Grain Shift (RGS) and RGS + relaxation methodologies [33–35]. In this approach, the equilibrium structures were first shifted along the direction normal

to the interface. At each displacement, a vacuum layer was added between the relevant IMC and Al at the interface. For each displaced structure, two kinds of calculations were performed: (1) RGS without any atomic relaxations, and (2) RGS + relaxation, where atomic positions were allowed to relax with the cell size fixed. For the RGS + relaxation methodology, the interface structure was separated along the normal direction by introducing a vacuum, and then DFT calculations were performed by allowing relaxation of atomic positions. The introduced strain between the two surfaces was increased with equal steps until the two phases fractured and split into two free surfaces. During the relaxation process for the RGS + relaxation methodology, the top two layers of Al and IMCs were fixed, such that during relaxation, atoms will not converge into another interface structure by relaxation of atomic positions into the vacuum layer introduced at the top of the structures. Fig. 4 illustrates the procedure for the tensile separation for the RGS + relaxation methodology. Each interface structure is divided into three regions. In the first region atoms are fixed and do not move during atomic relaxation, while in the second region, atoms are allowed to relax. The third region is defined as the tensile elongation region, where the vacuum layer is introduced between the two phases to mimic tensile behavior. Ideally, tensile calculations should be performed by introducing strain and allowing the structure to relax by optimizing the lateral lattice parameters to consider Poisson's effect. However, this methodology is very time-consuming and computationally expensive. Besides, the structural relaxation becomes difficult to converge for large strain values [35]. For these reasons, we did not consider Poisson's effect in this study.

The energy-displacement data obtained from the virtual tensile tests were fitted with the so-called Universal Binding Energy Relationship (UBER) [36,32,37]. Rose et al. [38] suggested that the binding energy of metals has a universal form of the kind given as;

$$E_b(d) = |E_b^e| \cdot g(a) \tag{2}$$

where E_b^e is the binding energy of the equilibrium structure, d is the displacement and a is the re-scaled displacement given as, $a = d/l$, where l is a characteristic length, depending on the curvature of the energy-volume curve at its minimum,
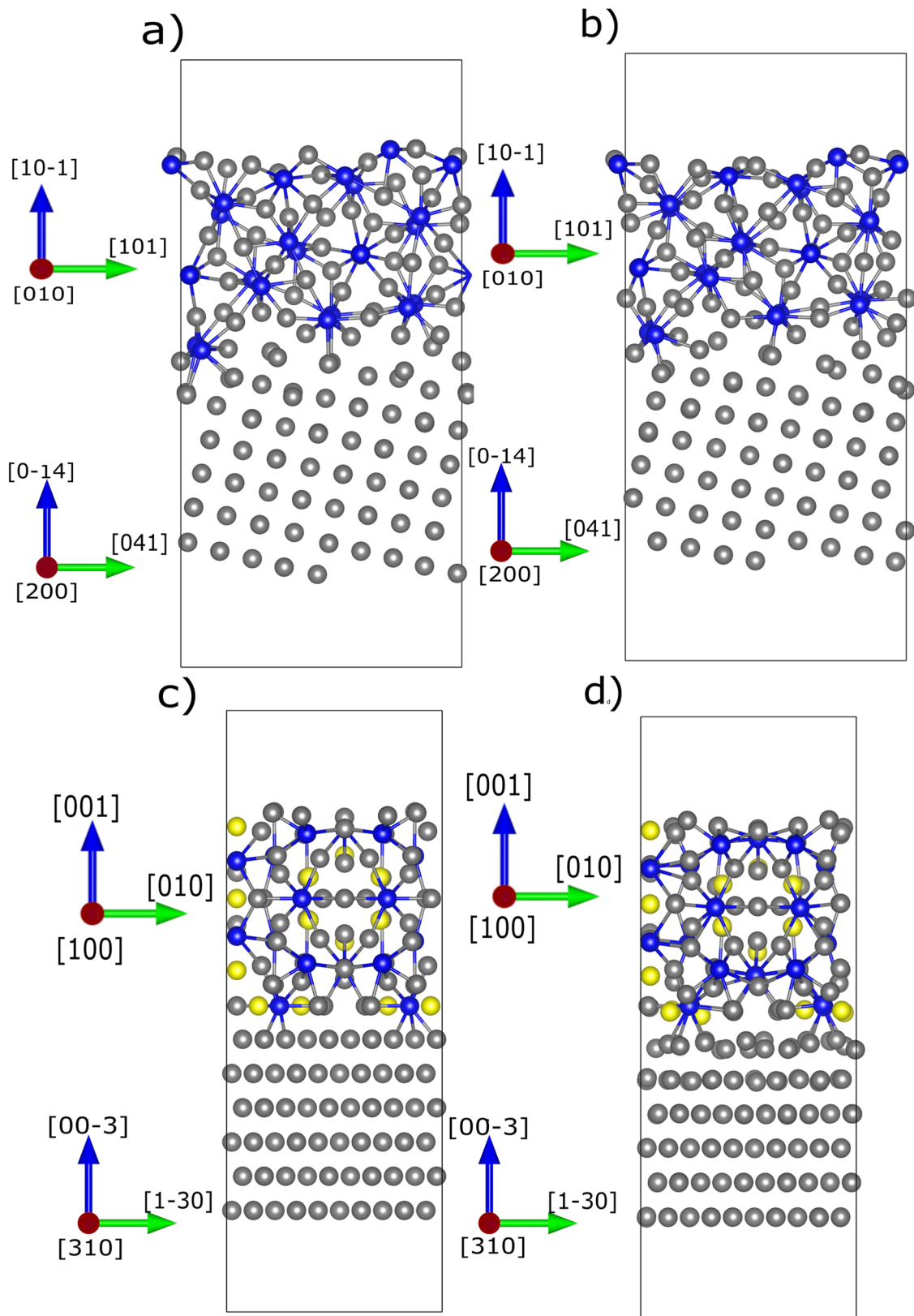
Fig. 2. The interface structure of Al//Fe$_4$Al$_{13}$ (a, b) and Al//α-AlFeSi (c, d). (a, c) show the interface structures before relaxation, while (b,d) show the structures after relaxation, for which the minimum forces on ions were reduced to < 0.01 eV/Å.

$$l = \sqrt{\frac{|E_b^e|}{E_b''(0)}}$$

(3)

If the functional form $g(a)$ is known, we can determine the

theoretical strength and critical displacement of any material from the parameters E_b^e and E_b''. For the hydrostatic compression/expansion, $g(a)$ is determined to have the following mathematical form [39]:

Table 3
The ideal work of separation, W_{sep}, of the Al//α-AlFeSi and Al//Fe$_4$Al$_{13}$ interfaces and bulk in units of J/m^2. (0) represent the crack opening at the interface, and (+1), (+2), and (+3) and (−1), (−2), and (−3) represent the crack opening at the 1st, 2nd and 3rd atomic layers of Al and IMC (α-AlFeSi and Fe$_4$Al$_{13}$), respectively, counting from the interface (0), while bulk Al, bulk IMC are the W_{sep} of pure Al and IMCs, respectively.

	Al// α-AlFeSi	Al// Fe$_4$Al$_{13}$	Al// Fe
bulk IMC	2.90 (α-AlFeSi)	3.17 (Fe$_4$Al$_{13}$)	–
−3	3.42 (α-AlFeSi)	3.46 (Fe$_4$Al$_{13}$)	–
−2	3.64 (α-AlFeSi)	1.15 (Fe$_4$Al$_{13}$)	–
−1	3.20 (α-AlFeSi)	4.08 (Fe$_4$Al$_{13}$)	–
0	2.26	2.21	5.84[a]
+1	1.90 (Al)	1.997 (Al)	–
+2	1.82 (Al)	2.06 (Al)	–
+3	1.9 4 (Al)	2.21 (Al)	–
bulk Al	2.07(1.8[b])	2.10(2.10[b])	1.8[b]

[a] [31] [b] [32].
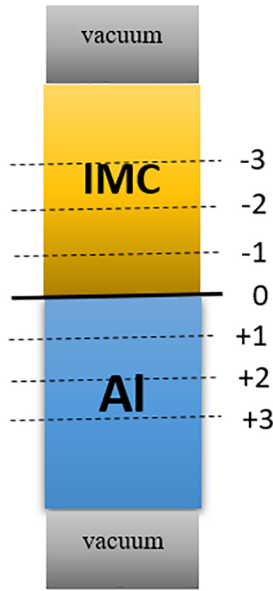
Fig. 3. Schematic illustration of W_{sep}. W_{sep} is calculated for fracture taking place at the interface (0), at the first layer (+ 1) of the Al side or the IMC side (− 1), as well as at the second and third layers, W_{sep} is defined at +2(Al), −2 (IMC), and +3 (Al), −3(IMC) respectively.

$$g(a) = -(1 + a + P(a))e^{-a - Q(a)} \qquad (4)$$

where P and Q are polynomials of order two or larger. This expression for $g(a)$ ensures that $g(0) = -1$, $g(a \to \infty) = 0$ and $g'(0) = 0$. The first-order terms are excluded from P and Q since they are related to each other as well as to the characteristic length [39].

By differentiating Eq. (2), the theoretical tensile strength of the atomic structures can be evaluated [36];

$$\sigma_{th} = \frac{\partial E_b}{\partial d} \qquad (5)$$

The maximum value of the theoretical strength σ_{th} is defined as the Ultimate Tensile Strength (σ_{UTS}), and the displacement at which σ_{UTS} is achieved is defined as the critical length d_c.

For the Al//α-AlFeSi interface, a good fit was found during RGS calculations. During RGS + relaxation calculations, higher-order polynomials were also considered. Although we found a reasonable fit using a fifth order polynomial, it does not fit the data for higher displacements. To find a good fit at higher displacements, we included an additional odd-order term for the RGS + relaxation methodology.

Appendix Tables 6 and 7 list the terms and coefficient values for both methodologies.

Similarly, for the case of the Al//Fe$_4$Al$_{13}$ interface, higher-order polynomials were used to fit the RGS + relaxation curve. The results obtained from the UBER fit are explained in the following subsections.

3.3. Rigid virtual tensile tests

Starting from the optimized structures, virtual compression and virtual tensile tests were performed as mentioned in subsection 3.2 without atomic relaxation. The energy increase for the compression tests was also calculated. Fig. 5(a) and (b) shows the virtual tensile test results for Al//α-AlFeSi and Al//Fe$_4$Al$_{13}$ interface structures strained along the normal [1 0 0] and [1 0 $\bar{1}$] directions, respectively. Values of E_b^e and l as defined by the UBER form in Eq. (2) for the Al//α-AlFeSi interface are 2.26 J/m^2 (0.14 eV/Å^2 = 2.26 J/m^2) and 0.317 Å, respectively, and those for Al//Fe$_4$Al$_{13}$ are 2.21 J/m^2 and 0.643 Å, respectively (Table 4). As can be seen in Fig. 5(a), at small tensile separations, a parabolic dependence of the binding energy is observed. With increasing displacement, there is a continuous increase in binding energy. The rate of this increase gets lower as the tensile displacement increases until it saturates at larger displacements of the fracture surfaces. Moreover, the UBER results fit well for the RGS methodology. From Fig. 5(a), we can see that the Al//α-AlFeSi interface has a slightly lower binding energy value (0.14 eV/Å^2) than Al//Fe$_4$Al$_{13}$ (0.1376 eV/Å^2), which indicates marginally stronger resistance to interfacial fracture for the Al//α-AlFeSi interface as compared to Al//Fe$_4$Al$_{13}$. The theoretical strength can be calculated from the fitted binding energy curve.

The theoretical stress-strain relations of the Al//α-AlFeSi and Al//Fe$_4$Al$_{13}$ interfaces are plotted in Fig. 5(b). To make comparisons with other studies, we performed additional virtual tensile tests for Al (2 1 0) bulk as well. As given in Table 4, σ_{UTS} for Al (2 1 0) bulk was found to be lower than σ_{UTS} of both Al//Fe$_4$Al$_{13}$ and Al//α-AlFeSi interface structures. This shows that during virtual tensile testing, the fracture is more likely to occur in the bulk aluminum side than at the interface. Since RGS virtual tensile testing was performed by rigidly separating the two surfaces from the interface, this result is consistent with our previous calculations.

Since Fe$_4$Al$_{13}$ and α-AlFeSi IMCs are stronger than aluminum, bonding of these strong IMCs with Al could be the reason for the higher interfacial strength. Furthermore, Al//Fe$_4$Al$_{13}$ showed lower σ_{UTS} (12.81 GPa) than Al//α-AlFeSi (17.76 GPa). Generally, the trend in σ_{UTS} follows the W_{sep} values: the higher W_{sep}, the higher σ_{UTS} value [37]. The same trend can be found for Al//Fe$_4$Al$_{13}$ and Al//α-AlFeSi interface structures. However, σ_{UTS} obtained from RGS virtual tests are most probably overestimated, which is why relaxed-type RGS virtual tensile tests were also performed. Such virtual tests are discussed in the following subsection.

3.4. Relaxed virtual tensile tests

In the relaxed-type virtual tensile tests, atoms were allowed to relax during the virtual tensile tests. Fig. 6(a) and (b) show the binding energy versus displacement curve for the Al//Fe$_4$Al$_{13}$ and Al//α-AlFeSi interfaces, evaluated by the RGS + relaxation methodology. Close to the 0 eV/Å^2 binding energy where the interface structures are separated into slabs, bulk atoms relax into minimum energy configuration in the RGS + relaxation methodology, hence the reference structure is different for RGS and RGS + relaxation methodologies at the same tensile displacement.

The equilibrium binding energy E_b^e during RGS virtual tensile tests can also be characterized as the energy required to separate an interface structure into two free surfaces ($E_b(0) = -W_{sep}$). In the case of RGS + relaxation virtual tests, this energy corresponds to the energy needed to separate an interface into two relaxed surfaces. As the interfaces are separated along the normal direction, we see that the
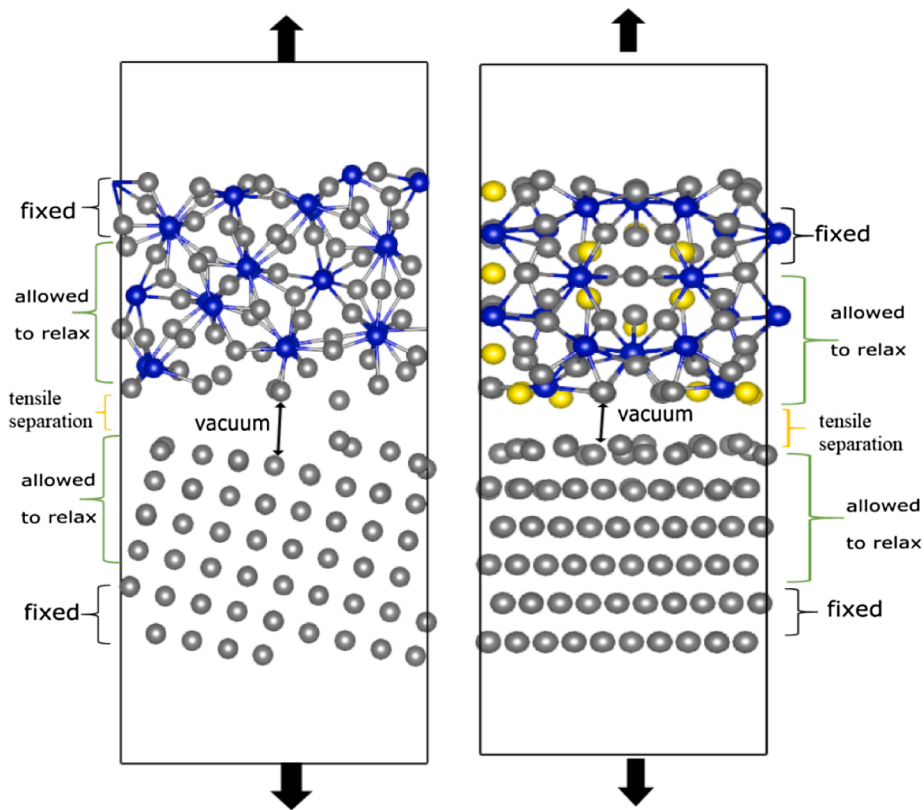
Fig. 4. Schematic illustration of the tensile elongation for the RGS + relaxation methodology. for the compression test, equilibrium structures are moved toward each other.

binding energy asymptotically reaches separating energy. From the RGS + relaxation methodology, we can also determine the tensile limit beyond which the pre-crack introduced during tensile displacement can no longer be healed.

The binding energy curve is divided into three distinct regions [36]: Region I: ($d < d_c$): the pre-crack introduced during tensile separation is healed up by elastic relaxations for small displacements, and surfaces will be reconnected, Region II ($d_c < d < d_f$): the so-called instability region, where the crack can neither be healed nor are the interface structures completely separated, and Region III ($d > d_f$): at larger displacements, the interface structure is fractured and the corresponding surfaces are completely separated.

Table 4 lists d_c and d_f for both interface structures. There is no unique way of defining final fracture length d_f, but we define it to be the displacement where the binding energy reaches -0.003 eV/Å^2. The range of the instability region gives indications of the brittleness and ductility of the interface structures and is defined by the difference between d_f and d_c. Al//α-AlFeSi has a lower range of the instability region (0.86 Å) as compared to Al//Fe$_4$Al$_{13}$ (1.43 Å), which indicates that the former interface is more brittle than the latter one.

3.5. Theoretical tensile strength

Table 4 lists all the calculated values of σ_{UTS} for the Al//Fe$_4$Al$_{13}$ and Al//α-AlFeSi interface structures, obtained by both the RGS and RGS + relaxation methodologies. The RGS + relaxation type tensile calculations show a lower tensile strength than the RGS tensile calculations. This is due to the fact that increased degrees of freedom during the atomic relaxation increases the possibility of failure initiation.

The maximum value of the stress-strain curve i.e. σ_{UTS} for Al//Fe$_4$Al$_{13}$ is 13.17 GPa as compared to 17.27 GPa for the Al//α-AlFeSi interface structure in the RGS methodology. As expected, the RGS + relaxation type virtual tensile tests show lower tensile strength

at larger critical length values. The larger d_c value for the RGS + relaxation methodology is caused by the stretching of the whole system [40]. The Al//Fe$_4$Al$_{13}$ interface shows higher critical length than the Al//α-AlFeSi interfaces for both methodologies. As given in Table 4, d_c is significantly higher in the case of RGS + relaxation methodology than the RGS method for all structures.

Similarly, the Al//Fe$_4$Al$_{13}$ interface shows lower σ_{UTS} (9.85 Å) than the Al//α-AlFeSi (10.92 Å) interface during RGS + relaxation. As discussed in the previous subsection, the higher strength is caused by the movement of Al atoms during elastic relaxation. Generally, the failure should preferentially initiate at the interfacial Al-Al in the Al//Fe$_4$Al$_{13}$ interface (region I in Fig. 8) and at Si-Al for the Al//α-AlFeSi interface (region I in Fig. 7) due to the weak bonding zone. This crack formation mechanism will be further elucidated in the next subsection.

The tensile strength of the Al(210) plane was calculated separately, and the results are reported in Table 4. It is worth noting that our RGS + relaxation calculations show good agreement with Zhang et al. [41] and Černỳ et al. [42]. Comparing the bulk Al mechanical strength with IMC interfaces show that the Al bulk side is the weakest zone of the overall interface structure. Incorporation of Poisson's effect in uniaxial tensile tests will most probably reduce σ_{UTS}. However, as mentioned earlier, due to the limited number of atoms and the computational costs associated with it, we did not consider Poisson's contraction in our ab initio tensile calculations.

3.6. Charge density

The fracture behavior of the RGS + relaxation type virtual tensile tests can be analyzed further by the electronic charge density of the interface structures. As shown in Fig. 7, in the stable configuration, the interfacial Si atoms face Al and Fe atoms, and the charge density between Si and Fe atoms is relatively high on the upper layers of α-AlFeSi. There is a charge depletion region between interfacial Al-Si atoms, as
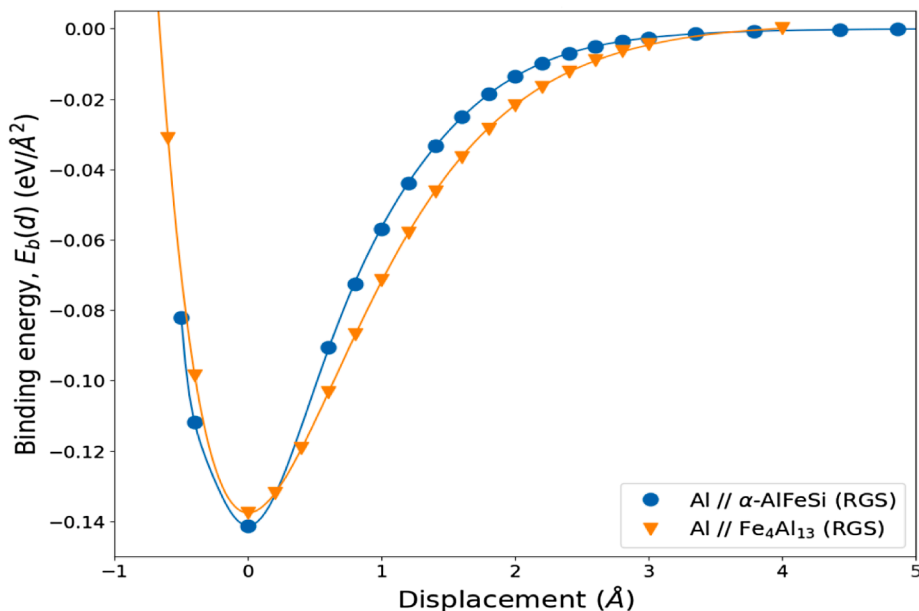
(a) Binding energy versus interfacial separation.
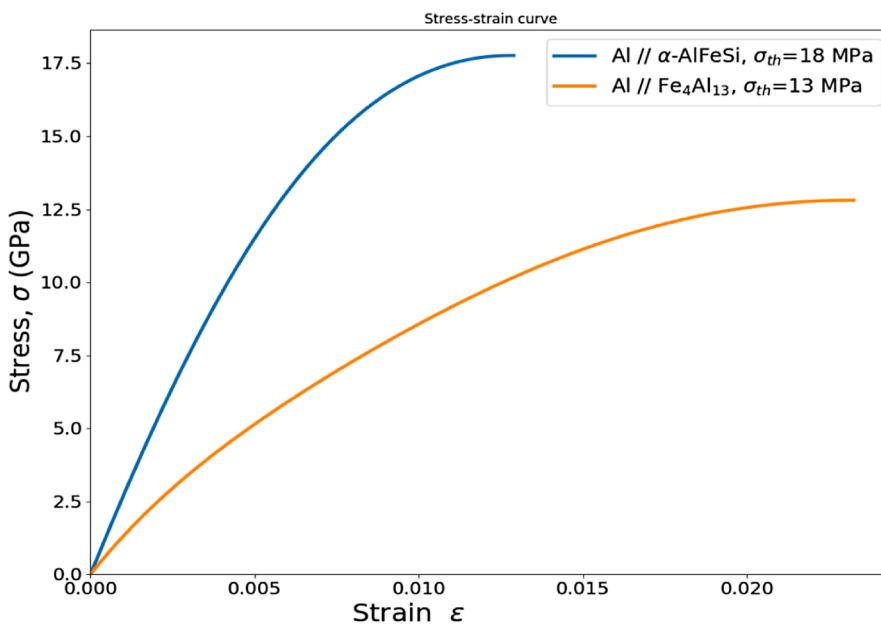
(b) Stress-strain curve

Fig. 5. (a) RGS virtual tensile tests for the Al//α-AlFeSi and the Al//Fe$_4$Al$_{13}$ interface structures. The solid curve represents the fitting of the universal binding-energy relation (UBER) (b) Stress-strain curve plotted by differentiating the UBER curves given in (a), up to the value of the strain corresponding to σ_{UTS}.

shown in region I in Fig. 7. This charge depletion region increases with the increase in tensile displacement. At 2.4 Å displacement of Al//α-AlFeSi interface, the charge density between interfacial Al-Al atoms is higher than that of the interfacial Si-Al pair. This indicates that bonding between interfacial Si-Al is weaker than the interfacial Al-Al bonding. As the tensile displacement increases, interfacial Si atoms move towards α-AlFeSi, and charge depletion region I increases, until the interface structure splits into two surfaces at a displacement of ~2.8 Å.

In the case of the Al//Fe$_4$Al$_{13}$ interface structure shown in Fig. 8, we can see higher charge density regions between Fe-Al atoms at the equilibrium configuration (0 Å) on the second layer of Fe$_4$Al$_{13}$. The charge depletion region at zero displacement can be seen between interfacial Al-Al atoms as well. Charge depletion regions are marked as regions I and II at 1.8 Å. As the tensile displacement increases, these

depletion regions grow in size. The depletion region marked as II, which can also be seen at 0.0 Å and 1.8 Å, is reconnected by elastic relaxation at a displacement of 2.6 Å, but depletion region I still grows in size. This shows that the Al atoms move towards the Fe atoms during tensile separation. At a tensile displacement of 3.0 Å, we can see that the depletion regions have become wide, but still, the charge density is relatively large between interfacial Al-Al atoms, which exhibit large resistance to complete interfacial separation. The Al//Fe$_4$Al$_{13}$ interface structure splits up into two free surfaces at d_f (~3.13 Å).

On the Fe$_4$Al$_{13}$ side in Fig. 8, we can see a spherically shaped charge depletion region at the second layer. This depletion region can explain the lower W_{sep} value at the second layer of the Fe$_4$Al$_{13}$ side, as discussed in subsection 3.1. This is also a very interesting observation, which shows that Fe$_4$Al$_{13}$ could be very anisotropic and brittle due to the

Table 4
Ultimate tensile strength and fitting parameters of Al(210) bulk, Al//α-AlFeSi and Al//Fe$_4$Al$_{13}$ calculated by RGS and RGS + relaxation methodologies. d_c, d_f and l are the critical length, final fracture length and characteristic length.
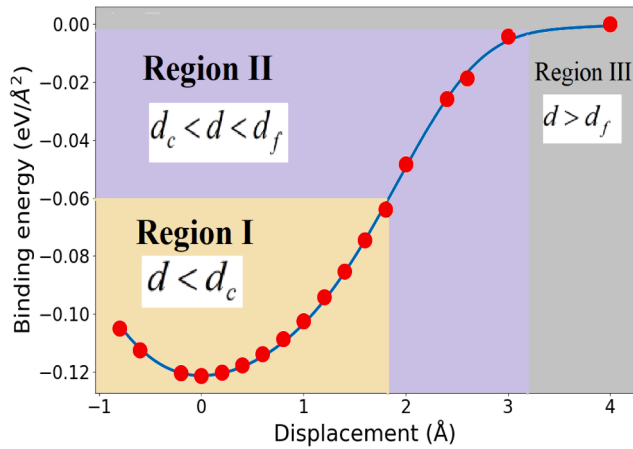
Interface	Rigid shift (RGS) σ_{UTS} (GPa)	RGS + relaxation σ_{UTS} (GPa)	d_c (Å)	l (Å)	d_f (Å)
Al(210)	10.11	8.99	1.45[a]	1.471[a]	6.20[b]
	11.96[36]	9.39[36]	3.03[b]	2.810[b]	
		8.40[41]			
Al//Fe$_4$Al$_{13}$	13.17	9.85	0.6[a]	0.643[a]	3.18[b]
			1.80[b]	1.483[b]	
Al//α-AlFeSi	17.27	10.92	0.43[a]	0.317[a]	2.86[b]
			1.94[b]	− 1.180[b]	

[a] RGS.
[b] RGS + relaxation.
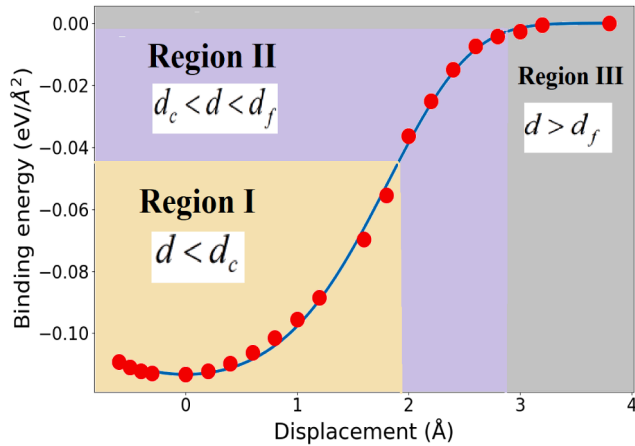
(a) Al//α-AlFeSi interface.

(b) Al//Fe$_4$Al$_{13}$ interface.

Fig. 6. Binding energy versus tensile displacement of (a) Al//α-AlFeSi and (b) Al//Fe$_4$Al$_{13}$ interfaces in RGS + relaxation type virtual tensile tests.

existence of such weak zones. Comparing Figs. 7 and 8, the Al//Fe$_4$Al$_{13}$ interface splits up at a larger tensile displacement than the Al//α-AlFeSi interface, which again confirms the longer range of the instability region for the Al//Fe$_4$Al$_{13}$ interface structure.

The long range of charge decay at the atomic scale for the Al//Fe$_4$Al$_{13}$ interface allows atoms to find alternate modes of energy dissipation, such as atomic stretching to bridge the void. At the macroscopic level, this behavior can result in the formation of dislocation planes over crack-tip propagation [43].

3.7. Ideal shear strength

To calculate the ideal shear strength of Al//IMC interfaces, a series of incremental strains were introduced along the **x**- and **y**-directions, respectively. For the Al(001)//α-AlFeSi(001) interface, the atoms of α-AlFeSi were rigidly moved along the [010] and [100] directions by keeping the cell size fixed. Similarly for the Al//Fe$_4$Al$_{13}$ interface, Fe$_4$Al$_{13}$ layers were moved along the [010] and [101] directions, respectively, as shown in Fig. 9(a–d). During shear calculations, atoms were allowed to relax along the normal direction to the interface. Furthermore, to avoid periodic interaction between structures, a vacuum layer of > 10 Å was added for all interfaces. Shear stress was calculated and plotted as a function of shear displacement along defined slip directions according to the following Fourier series expression,

$$E_s(d) = E_0 + \sum_{i=1}^{\infty} [A_i cos(k_i d) + B_i sin(k_i d)] \tag{6}$$

where $E_s(d)$ and E_0 are the energy of the displaced and reference structure respectively, and $k_i = \frac{2\pi i}{\lambda}$, where λ is the periodicity along the shear direction.

Due to the periodicity of the crystal structure along the shear direction, a Fourier series was used to fit shear stress-displacement data. The shear stress is calculated as;

$$\gamma_s = \frac{1}{A} \frac{\partial E_s}{\partial d} \tag{7}$$

where A is the area of the interface structures.

We used a Fourier series of order $n = 3$ to fit the shear stress-displacement curve. The shear stress-displacement curve fits well with the Fourier series Eq. (6), as can be seen in Fig. 10(a) and (b) for both interface structures.

Fig. 10 shows the stress-displacement curves for the Al//α-AlFeSi and Al//Fe$_4$Al$_{13}$ interface structures as a function of shear displacement along the shear directions. Table 5 summarizes the shear strength of various slip systems of interface structures considered in this study. As can be seen in Fig. 10, the stress increases initially until it reaches a maximum value. The maximum is defined as the ideal shear strength of the interface structures in this study (γ_{max}). For the Al//α-AlFeSi interface, the most favorable slip direction is found to be along $\langle 010 \rangle$ with the ideal shear strength value of 2.23 GPa, while higher strength was found along the $\langle 100 \rangle$ shear direction (3.14 GPa). The Al//Fe$_4$Al$_{13}$ interface shows higher strength with the highest value found along the $\langle 010 \rangle$ direction (7.65 GPa) while lower along $\langle 101 \rangle$ direction (5.11 GPa). Based on these values, it can be concluded that the Al//Fe$_4$Al$_{13}$ interface has higher shear strength as compared to the Al//α-AlFeSi interface.

The atoms at the Al//α-AlFeSi interface are aligned in a straight line, as can be seen in Fig. 9(a) and (b). During the shearing process along the [010] and [100] directions, these atoms do not face any energy barrier caused by other atoms. However, in the case of the Al//Fe$_4$Al$_{13}$ interface, atoms are aligned in a zig-zag manner at the interface along the [010] direction (Fig. 9(c)), which creates a barrier during the shearing process. The maximum shear strength is achieved when this energy barrier has been overcome by the shearing displacement along the particular slip direction. This causes the higher shear strength for the Al//Fe$_4$Al$_{13}$ interface along the [010] direction. Lower strength has been found along the [101] direction due to the straight alignment of atoms at the interface.

4. Discussion

Virtual tensile and shear calculations were performed to selected Al//IMC structures and thereby obtaining insights into the governing mechanisms of Fe$_4$Al$_{13}$ and α-AlFeSi intermetallics at aluminum and steel joints. To our best knowledge, this paper contains the first detailed
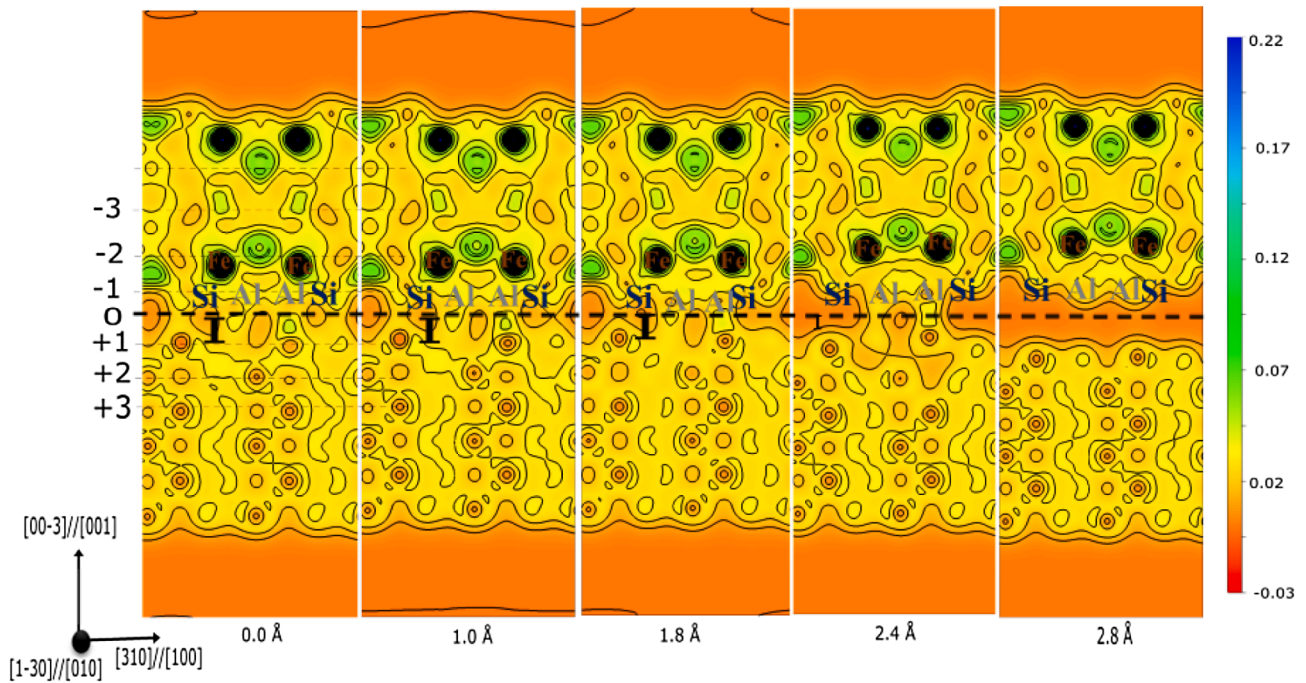
Fig. 7. Calculated charge density of the Al//α-AlFeSi interface during increased displacement (d), evaluated in the RGS + relaxation methodology in units of e/Å^3. Atomic layers (± 1, ± 2, ± 3) are marked as per the definition of Fig. 3.

first-principles study of Al//Fe$_4$Al$_{13}$ and Al//α-AlFeSi intermetallic interfaces.

Calculations of W_{sep} gave indications of the location of the weakest zone of the interface and the bulk sides. Interestingly, the second layer of Fe$_4$Al$_{13}$ was found to be the weakest zone of the whole Al//Fe$_4$Al$_{13}$ structure, as discussed in Section 3.1. Charge density plots indicated a charge depletion region around Fe atoms at the second layer of the Fe$_4$Al$_{13}$ intermetallic side (Fig. 8). Although Fe$_4$Al$_{13}$ seems to have the highest strength, the presence of this weak zone is a possible explanation of the highly anisotropic behavior of the Fe$_4$Al$_{13}$ layers. Therefore, it can be suggested from these calculations that micro-cracks are more likely to develop in Fe$_4$Al$_{13}$ due to the presence of charge depletion regions. On the other hand, α-AlFeSi showed consistent values of W_{sep} (Table 3). The α phase showed higher W_{sep} values, which indicates that this phase has stronger bonding characteristics as compared to the

Fe$_4$Al$_{13}$ phase and less likely to induce micro-cracks. Generally, the Al side was found to be softer than the intermetallic layers except for the second layer of Fe$_4$Al$_{13}$. At the interface, the Al//α-AlFeSi interface showed a higher W_{sep} value (2.26 J/m^2) than Al//Fe$_4$Al$_{13}$, which is an indication of higher mechanical strength.

Tensile calculations of these interface structures also agree with the W_{sep} values. The Al//α-AlFeSi interface showed higher interfacial strength as compared to the Al//Fe$_4$Al$_{13}$ interface structure. Charge density plots indicated that the Si atoms at the interface tend to induce cracks at the interface side, while Al atoms seem to have stronger bonding with interfacial Al atoms. Similarly for the Al//Fe$_4$Al$_{13}$ interface, Fe atoms of the Fe$_4$Al$_{13}$ phase seem to have stronger bonding strength with the interfacial Al atoms. Hence it is reasonable to suggest that the presence of Fe atoms at the interface produces stronger bonding than Al and Si atoms. Al atoms tend to show more ductile

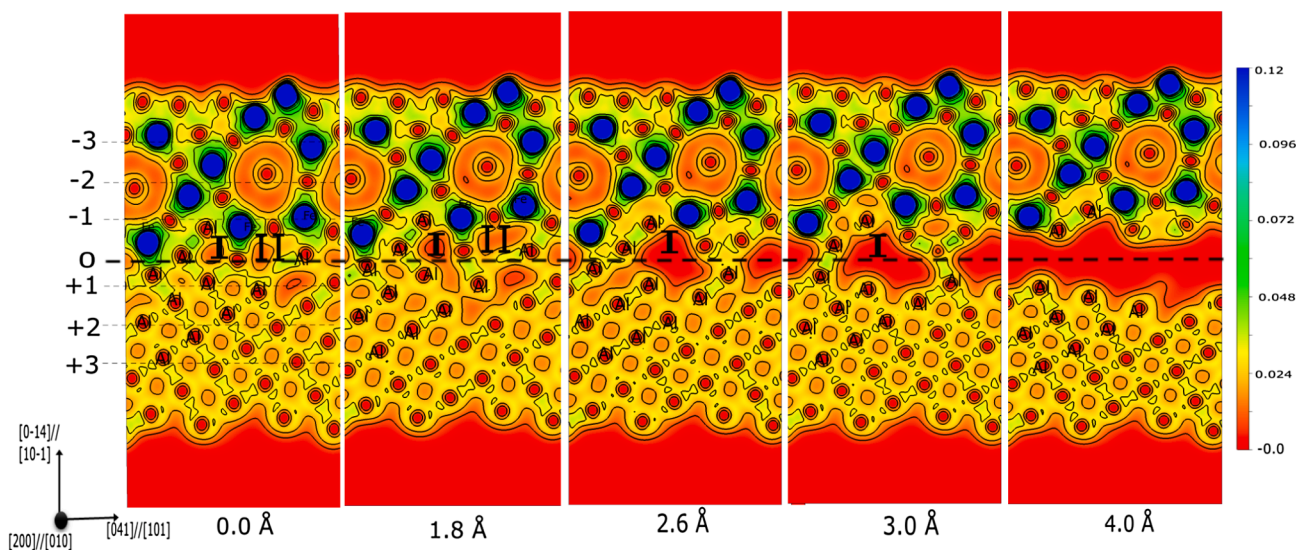**Fig. 8.** Calculated charge density of Al//Fe$_4$Al$_{13}$ interface during increased displacement (d), evaluated in the RGS + relaxation methodology in units of e/Å^3. Atomic layers (± 1, ± 2, ± 3) are marked as per the definition of Fig. 3.
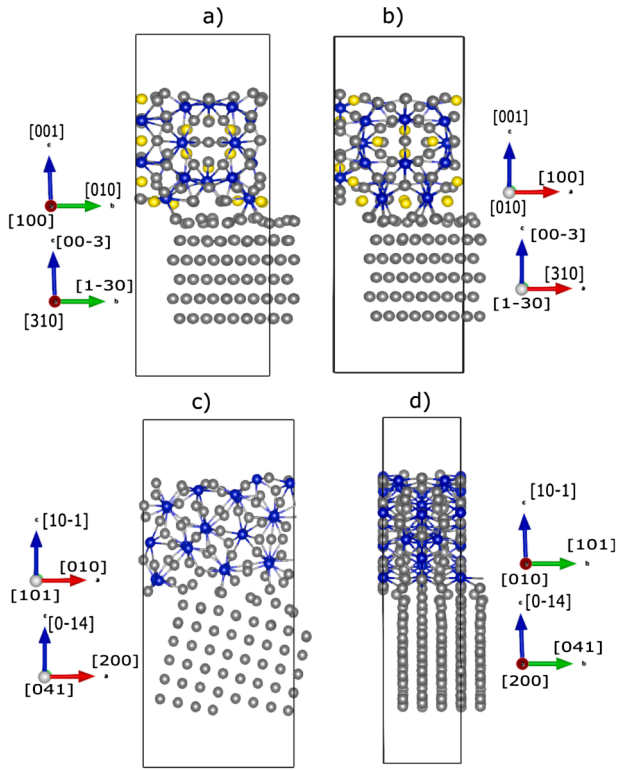
Fig. 9. Schematic illustration of the directions of shear for Al//α-AlFeSi (a, b) and Al//Fe$_4$Al$_{13}$ (c, d).

Table 5
Ideal shear strength of the Al//α-AlFeSi and Al//Fe$_4$Al$_{13}$ interfaces. Direction of shear is defined with respect to Al along $\langle 101 \rangle$ $\langle 010 \rangle$ and $\langle 100 \rangle$ direction.

Interface	γ_{max} $\langle 101 \rangle$ (GPa)	γ_{max} $\langle 010 \rangle$ (GPa)	γ_{max} $\langle 100 \rangle$ (GPa)
Al//α-AlFeSi	–	2.23	3.14
Al//Fe$_4$Al$_{13}$	5.11	7.65	–

5. Conclusions and outlook

We have developed and performed ab initio calculations of Al//Fe$_4$Al$_{13}$ and Al//α-AlFeSi interface structures. To characterize the interfacial strength, we calculated W_{sep} to find the weak zone of the interface structure. The Al//α-AlFeSi interface was found to have a higher W_{sep} value than the Al//Fe$_4$Al$_{13}$ interface. Besides, the W_{sep} values show that during uni-axial tension, the interface is most likely to fracture from the Fe$_4$Al$_{13}$ side with the lowest value reported to be 1.15 J/m^2 for the Al//Fe$_4$Al$_{13}$ interface. This low value of W_{sep} is caused by the spherical charge depletion region in the second layer (− 2) in Fe$_4$Al$_{13}$.

Furthermore, a series of tensile calculations were performed in the framework of the RGS methodology both with and without the relaxation of atomic positions at each shift. These tensile simulations yielded energy-displacement data, which were fitted by the UBER curve. Based on these calculations, the Al//Fe$_4$Al$_{13}$ interface structure has a lower ultimate tensile strength than the Al//α-AlFeSi interface. Shear strength calculations were also performed for the Al//Fe$_4$Al$_{13}$ structure along the $\langle 101 \rangle$ and $\langle 010 \rangle$ shear directions, and for Al//α-AlFeSi along $\langle 100 \rangle$ and the $\langle 010 \rangle$ directions. As displayed in Tables 4 and 5, the Al//α-AlFeSi interface showed higher tensile and lower shear strength as compared to the Al//Fe$_4$Al$_{13}$ interface structure.

It should be emphasized that the effects of temperature, boundaries, cracks, and dislocations have not been taken into account in this study. These defects dominate the failure behavior in reality. At the macroscopic level, the actual strain and stress values are usually small as compared to the ideal stress and strain values. Therefore it is necessary to find strategies to link ab initio calculations with the macroscopic failure process by Finite Element Modeling (FEM) and molecular dynamics simulations methods [44,45]. This study is part of a larger project aiming at characterizing the role of IMCs at aluminum-steel joints, and we plan to use ab initio calculations as input for FEM simulations to predict the macroscopic behavior of aluminum-steel joints.

behavior than Fe atoms, which produce an energy barrier along the shearing direction. To have a shear along the particular shearing direction, the energy barrier created by the interfacial bonding has to be overcome by the shearing process. Al atoms create a higher energy barrier, and there are more Al atoms at the Al//Fe$_4$Al$_{13}$ interface than at the Al//α-AlFeSi interface, which is why the Al//Fe$_4$Al$_{13}$ interface shows a higher shear strength. From these calculations, it can be suggested that the presence of Fe atoms at the interface produces stronger tensile strength, while higher shear strength is achieved by the Al atoms at the interface.
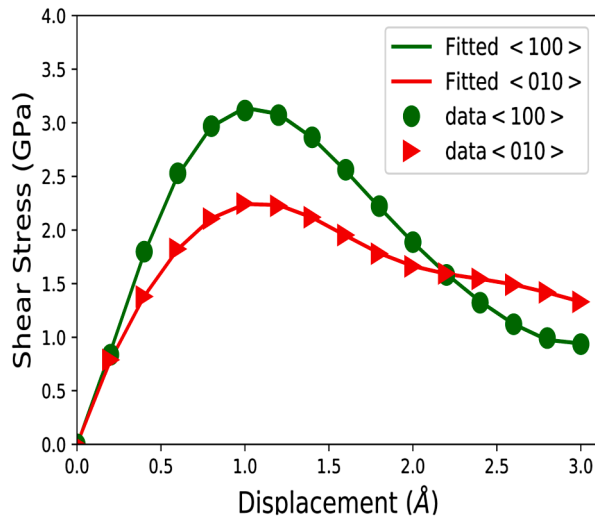
(a) Al (001)//α-AlFeSi(001) interface
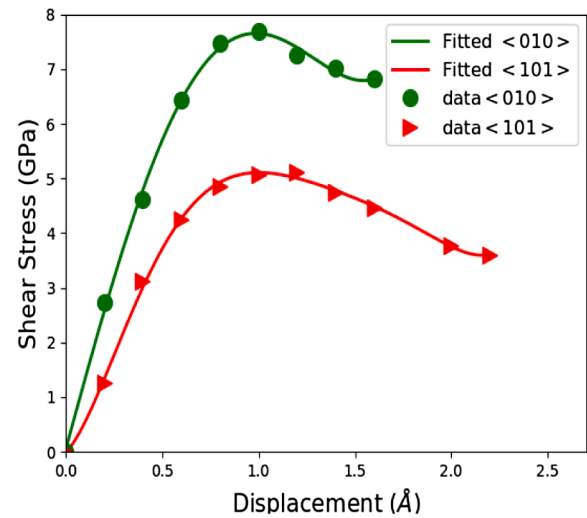
(b) Al (0$\bar{1}$4)//Fe$_4$Al$_{13}$ (10$\bar{1}$)

Fig. 10. Shear stress-displacement curve of the Al(00$\bar{3}$)//α-AlFeSi(001) and Al(0$\bar{1}$4)//Fe$_4$Al$_{13}$ (10$\bar{1}$) interfaces during the shear strength simulations as a function of shear displacement along different shear directions.

CRediT authorship contribution statement

Muhammad Zeeshan Khalid: Methodology, Conceptualization, Software, Data curation, Writing - original draft, Visualization, Investigation, Formal analysis, Writing - review & editing, Validation. **Jesper Friis:** Methodology, Software, Formal analysis, Supervision, Writing - review & editing, Conceptualization, Validation. **Per Harald Ninive:** Methodology, Software, Supervision, Resources, Writing - review & editing, Validation. **Knut Marthinsen:** Supervision, Project administration, Writing - review & editing, Validation. **Are Strandlie:** Formal analysis, Supervision, Project administration, Resources, Writing - review & editing, Funding acquisition, Validation.

Declaration of Competing Interest

The authors declare that they have no known competing financial interests or personal relationships that could have appeared to influence the work reported in this paper.

Acknowledgements

Appendix A

Tables 6 and 7.

Table 6
The fitting coefficient binding energy $E_b(d)$ values of the Al//Fe$_4$Al$_{13}$ interface.

Terms	1	2	3	4	5	7	9
RGS	0.0	-0.00542	-0.0247	0.00427	-0.000706	–	–
RGS + relaxation	1.7954	–	–	–	-0.324	0.0681	0.148

Table 7
The fitting coefficient binding energy $E_b(d)$ values of the Al// α-AlFeSi interface.

Terms	1	2	3	4	5	7	9
RGS	0.0	0.305	-0.00145	-0.0125	0.0.00359	–	–
RGS + relaxation	6.232	–	–	–	-40.9955	4.029	47.229

References

[1] H. Wargnier, F. Kromm, M. Danis, Y. Brechet, Proposal for a multi-material design procedure, Mater. Des. (1980–2015) 56 (2014) 44–49.
[2] T. Netland, J. Ravn, G. Knutstad, L. Skjelstad, Idealfactory@ xps: a manufacturing concept for high-tech norwegian companies, 2011.
[3] J. Pflug, I. Verpoest, Sandwich materials selection charts, J. Sandwich Struct. Mater. 8 (2006) 407–421.
[4] G.N. Levy, R. Schindel, J.-P. Kruth, Rapid manufacturing and rapid tooling with layer manufacturing (LM) technologies, state of the art and future perspectives, CIRP Ann.-Manuf. Technol. 52 (2003) 589–609.
[5] M. Bahraminasab, B. Sahari, K. Edwards, F. Farahmand, T.S. Hong, M. Arumugam, A. Jahan, Multi-objective design optimization of functionally graded material for the femoral component of a total knee replacement, Mater. Des. 53 (2014) 159–173.
[6] M. Pourali, A. Abdollah-Zadeh, T. Saeid, F. Kargar, Influence of welding parameters on intermetallic compounds formation in dissimilar steel/aluminum friction stir welds, J. Alloys Compd. 715 (2017) 1–8.
[7] J.M. Piccini, H.G. Svoboda, Effect of pin length on friction stir spot welding (FSSW) of dissimilar Aluminum-Steel joints, Proc. Mater. Sci. 9 (2015) 504–513.
[8] K. Martinsen, S. Hu, B. Carlson, Joining of dissimilar materials, CIRP Ann. 64 (2015) 679–699.
[9] P. Liu, G. Dunlop, Crystallographic orientation relationships for Al-Fe and Al-Fe-Si precipitates in aluminium, Acta Metall. 36 (1988) 1481–1489.
[10] M. Potesser, T. Schoeberl, H. Antrekowitsch, J. Bruckner, The characterization of the intermetallic Fe-Al layer of steel-aluminum weldings, in: EPD Congress, vol. 1, San Antonio Texas, USA, p. 167.
[11] X. Liu, S. Lan, J. Ni, Analysis of process parameters effects on friction stir welding of dissimilar aluminum alloy to advanced high strength steel, Mater. Des. 59 (2014) 50–62.
[12] S. Bozzi, A. Helbert-Etter, T. Baudin, B. Criqui, J. Kerbiguet, Intermetallic compounds in Al 6016/IF-steel friction stir spot welds, Mater. Sci. Eng.: A 527 (2010) 4505–4509.
[13] Y. Sun, H. Fujii, N. Takaki, Y. Okitsu, Microstructure and mechanical properties of dissimilar Al alloy/steel joints prepared by a flat spot friction stir welding technique, Mater. Des. 47 (2013) 350–357.
[14] N. Chen, H.-P. Wang, B.E. Carlson, D.R. Sigler, M. Wang, Fracture mechanisms of Al/steel resistance spot welds in lap shear test, J. Mater. Process. Technol. 243 (2017) 347–354.
[15] E. McDevitt, Y. Morimoto, M. Meshii, Characterization of the Fe-Al interfacial layer in a commercial hot-dip galvanized coating, ISIJ Int. 37 (1997) 776–782.
[16] K.-K. Wang, L. Chang, D. Gan, H.-P. Wang, Heteroepitaxial growth of Fe$_2$Al$_5$ inhibition layer in hot-dip galvanizing of an interstitial-free steel, Thin Solid Films 518 (2010) 1935–1942.
[17] S.M. Arbo, T. Bergh, H. Solhaug, I. Westermann, B. Holmedal, Influence of thermomechanical processing sequence on properties of AA6082-IF steel cold roll bonded composite sheet, Proc. Manuf. 15 (2018) 152–160.
[18] M. Finnis, The theory of metal-ceramic interfaces, J. Phys.: Condens. Matter 8 (1996) 5811.
[19] C.-H. Zhang, S. Huang, J. Shen, N.-X. Chen, Structural and mechanical properties of Fe-Al compounds: an atomistic study by EAM simulation, Intermetallics 52 (2014) 86–91.
[20] Y. Liu, X. Chong, Y. Jiang, R. Zhou, J. Feng, Mechanical properties and electronic structures of Fe-Al intermetallic, Physica B 506 (2017) 1–11.
[21] M.Z. Khalid, J. Friis, P.H. Ninive, K. Marthinsen, A. Strandlie, DFT calculations based insight into bonding character and strength of Fe$_2$Al$_5$ and Fe$_2$Al$_5$ intermetallics at Al-Fe joints, Proc. Manuf. 15 (2018) 1407–1415.
[22] P.G. Gonzales-Ormeño, H.M. Petrilli, C.G. Schön, Ab-initio calculations of the formation energies of bcc-based superlattices in the Fe-Al system, Calphad 26 (2002) 573–582.
[23] G. Kresse, J. Furthmüller, Vienna Ab-initio Simulation Package (vasp), Vienna University, Vienna, 2001.
[24] P.E. Blöchl, Projector augmented-wave method, Phys. Rev. B 50 (1994) 17953.
[25] J.P. Perdew, K. Burke, M. Ernzerhof, Generalized gradient approximation made simple, Phys. Rev. Lett. 77 (1996) 3865.
[26] H.J. Monkhorst, J.D. Pack, Special points for brillouin-zone integrations, Phys. Rev. B 13 (1976) 5188.
[27] M. Cooper, The crystal structure of the ternary alloy α(AlFeSi), Acta Crystallogr. A 23 (1967) 1106–1107.
[28] A.M.F. Muggerud, Y. Li, R. Holmestad, Composition and orientation relationships of constituent particles in 3xxx aluminum alloys, Philos. Mag. 94 (2014) 556–568.
[29] I.G. Batyrev, A. Alavi, M.W. Finnis, Equilibrium and adhesion of Nb/sapphire: the effect of oxygen partial pressure, Phys. Rev. B 62 (2000) 4698.
[30] H. Guo, Y. Qi, X. Li, Adhesion at diamond/metal interfaces: a density functional theory study, J. Appl. Phys. 107 (2010) 033722 .
[31] M.Z. Khalid, J. Friis, P.H. Ninive, K. Marthinsen, A. Strandlie, A first-principles study of the Al (001)/Fe (0–11) interface, in: Materials Science Forum, vol. 941,

Trans Tech Publ, pp. 2349–2355.

[32] P. Lazar, R. Podloucky, Cleavage fracture of a crystal: density functional theory calculations based on a model which includes structural relaxations, Phys. Rev. B 78 (2008) 104114 .

[33] G. Zhang, M. Chen, Y. Shi, J. Huang, F. Yang, Analysis and modeling of the growth of intermetallic compounds in aluminum–steel joints, RSC Adv. 7 (2017) 37797–37805.

[34] A. Tahir, R. Janisch, A. Hartmaier, Hydrogen embrittlement of a carbon segregated $\sigma 5$ (310)[001] symmetrical tilt grain boundary in α-Fe, Mater. Sci. Eng.: A 612 (2014) 462–467.

[35] M. Yamaguchi, First-principles study on the grain boundary embrittlement of metals by solute segregation: Part i. iron (Fe)-solute (B, C, P, and S) systems, Metall. Mater. Trans. A 42 (2011) 319–329.

[36] D. Zhao, O.M. Løvvik, K. Marthinsen, Y. Li, Segregation of Mg, Cu and their effects on the strength of Al $\sigma 5$ (210)[001] symmetrical tilt grain boundary, Acta Mater. 145 (2018) 235–246.

[37] R. Janisch, N. Ahmed, A. Hartmaier, Ab initio tensile tests of al bulk crystals and grain boundaries: universality of mechanical behavior, Phys. Rev. B 81 (2010) 184108 .

[38] J.H. Rose, J.R. Smith, J. Ferrante, Universal features of bonding in metals, Phys. Rev. B 28 (1983) 1835.

[39] I.J. Jensen, J. Friis, C.D. Marioara, I.G. Ringdalen, The role of grain boundary precipitates during intergranular fracture in 6xxx series aluminium alloys, in preparation (????).

[40] R. Yang, S. Tanaka, M. Kohyama, First-principles study on the tensile strength and fracture of the Al-terminated stoichiometric α-Al$_2$O$_3$ (0001)/Cu (111) interface, Philos. Mag. 85 (2005) 2961–2976.

[41] S. Zhang, O.Y. Kontsevoi, A.J. Freeman, G.B. Olson, Sodium-induced embrittlement of an aluminum grain boundary, Phys. Rev. B 82 (2010) 224107 .

[42] M. Černỳ, P. Šesták, P. Řehák, M. Všianská, M. Šob, Ab initio tensile tests of grain boundaries in the fcc crystals of ni and co with segregated sp-impurities, Mater. Sci. Eng.: A 669 (2016) 218–225.

[43] E.A. Jarvis, R.L. Hayes, E.A. Carter, Effects of oxidation on the nanoscale mechanisms of crack formation in aluminum, ChemPhysChem 2 (2001) 55–59.

[44] J. Pask, P. Sterne, Finite element methods in ab initio electronic structure calculations, Modell. Simul. Mater. Sci. Eng. 13 (2005) R71.

[45] C.D. Berweger, W.F. van Gunsteren, F. Müller-Plathe, Molecular dynamics simulation with an ab initio potential energy function and finite element interpolation: the photoisomerization of cis-stilbene in solution, J. Chem. Phys. 108 (1998) 8773–8781.